An Investigation of the Fatigue and Fracture Behavior of a Nb-12Al-44Ti-1.5Mo Intermetallic Alloy

W.O. SOBOYEJO, J. DIPASQUALE, F. YE, C. MERCER, T.S. SRIVATSAN, and D.G. KONITZER

This article presents the results of a study of the fatigue and fracture behavior of a damage-tolerant Nb-12Al-44Ti-1.5Mo alloy. This partially ordered B2 + orthorhombic intermetallic alloy is shown to have attractive combinations of room-temperature ductility (11 to 14 pct), fracture toughness (60 to 92 MPa$\sqrt{m}$), and comparable fatigue crack growth resistance to IN718, Ti-6Al-4V, and pure Nb at room temperature. The studies show that tensile deformation in the Nb-12Al-44Ti-1.5Mo alloy involves localized plastic deformation (microplasticity *via* slip-band formation) which initiates at stress levels that are significantly below the uniaxial yield stress (~9.6 pct of the 0.2 pct offset yield strength (YS)). The onset of bulk yielding is shown to correspond to the spread of microplasticity completely across the gage sections of the tensile specimen. Fatigue crack initiation is also postulated to occur by the accumulation of microplasticity (coarsening of slip bands). Subsequent fatigue crack growth then occurs by the "unzipping" of cracks along slip bands that form ahead of the dominant crack tip. The proposed mechanism of fatigue crack growth is analogous to the unzipping crack growth mechanism that was suggested originally by Neumann for crack growth in single-crystal copper. Slower near-threshold fatigue crack growth rates at 750 °C are attributed to the shielding effects of oxide-induced crack closure. The fatigue and fracture behavior are also compared to those of pure Nb and emerging high-temperature niobium-based intermetallics.

I. INTRODUCTION

THE ongoing interest in the development of intermediate-temperature structural materials has stimulated considerable research on the use of niobium aluminide–based intermetallics for possible applications in the intermediate-temperature regime around 750 °C.[1–11] The interest in niobium aluminide–based intermetallics has been largely due to their attractive combinations of ductility and damage tolerance.[1–6] The oxidation resistance of niobium aluminide–based intermetallics has also been shown to be adequate for 750 °C aeroengine applications.[9] Their potential service temperature limit (of approximately 750 °C) is, therefore, below that of the niobium silicide[12,13,14] and the Laves phase[15,16] intermetallics that are being developed for potential high-temperature structural applications in the temperature regime above 1000 °C.

Nevertheless, with their moderate densities of ~6.1 g/cm^3,[6] niobium aluminides represent one of the promising alloy systems that have emerged from extensive alloy development efforts in recent years.[6,8,11] These efforts have shown that the addition of ~40 at. pct Ti to the A15 Nb-15Al (Nb_3Al) base promotes the stabilization of the B2 phase.[6] The stabilization of the B2 phase in the Nb-15Al-40Ti alloy was also shown to result in improved ductility (~10 to 30 pct) and fracture toughness (40 to 110 MPa$\sqrt{m}$).[4] Alloying with Mo, and a slight adjustment of the Al and Ti contents of the Nb-15Al-40Ti base, was also found to result in improved creep resistance and damage tolerance.[8] The alloy development efforts in Reference 8 resulted in an "optimal" B2 + orthorhombic alloy with a nominal composition of Nb-12Al-44Ti-1.5Mo.

This article presents the results of a study of the fatigue and fracture behavior of the Nb-12Al-44Ti-1.5Mo alloy (44Ti alloy). Following a brief description of material processing and microstructural features in Section II, the experimental details are presented in Section III. The micromechanisms of fracture and fatigue in smooth and notched specimens are then elucidated in Section IV, along with the associated mechanical property data. The implications of the results are examined in Section V, in which the fatigue and fracture properties of the 44Ti alloy are also compared to those of existing and emerging high-temperature structural alloys. Finally, salient conclusions arising from this work are summarized in Section VI.

II. MATERIAL

The 44Ti alloy that was used in this experimental study was supplied by Teledyne Wah Change (Albany, OR). It was produced by vacuum arc remelting techniques. The alloy was upset forged through five forging steps[8,11] to produce a billet that was approximately 30 × 240 × 150 mm in size. The nominal chemical composition of the as-forged ingot is provided in Table I. This was obtained using standard cumbostometric and spectroscopic techniques.

A typical optical micrograph of the as-forged 44Ti alloy is presented in Figure 1(a). This shows the elongated and ordered B2 grains (average grain size was ~200 μm in the transverse direction and approximately 600 μm in the longitudinal direction) in the as-forged material. The B2 structure of the as-received intermetallic material was verified by electron diffraction analysis during transmission elec-

W.O. SOBOYEJO, Associate Professor, J. DIPASQUALE, Graduate Student, and F. YE and C. MERCER, Postdoctoral Research Associates, are with the Department of Materials Science and Engineering, The Ohio State University, Columbus, OH 43210-1179. T.S. SRIVATSAN, Professor, is with the Department of Mechanical Engineering, the University of Akron, Akron, OH 44325-0002. D.G. KONITZER, Lead Engineer, is with General Electric Aircraft Engines, Cincinnati, OH 45215-1915.

Manuscript submitted May 7, 1998.

Table I. Actual Compositions of Nb-12Al-44Ti-1.5Mo Alloys (Atomic Percent)

Nb	Al	Ti	O	N	H	C	Cu	Mo
Balance	12.12	44.10	0.502	<0.023	0.223	0.054	<0.01	1.44

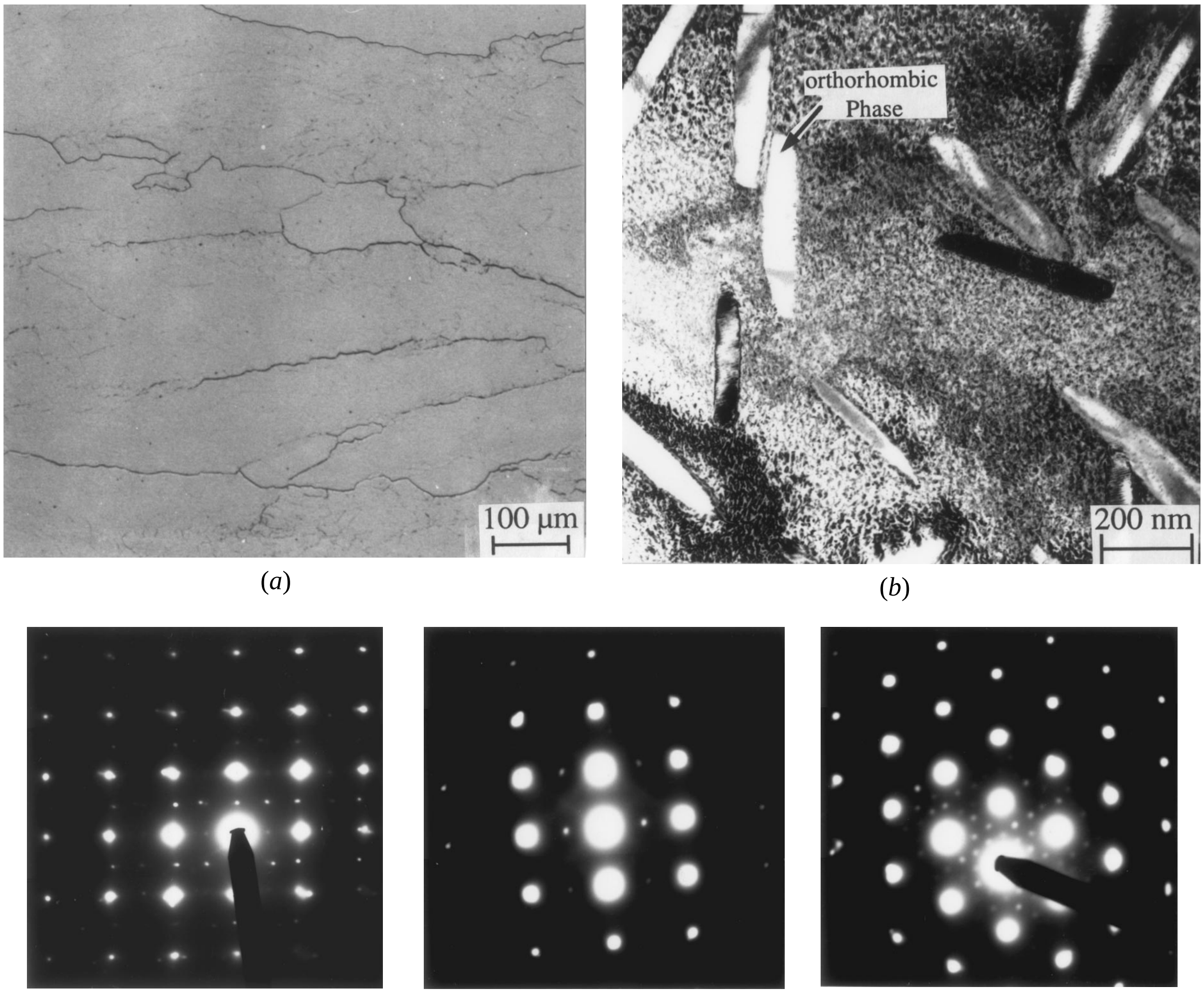

(*a*) (*b*)

(001) zone axis (*c*) (011) zone axis (*d*) (111) zone axis (*e*)

Fig. 1—Microstructure and structure of Nb-12A1-44Ti-1.5Mo intermetallic alloy; (*a*) as-forged, (*b*) TEM image of DA alloy, and (*c*) through (*e*) electron diffraction patterns obtained from DA alloy.

tron microscopy (TEM) of thin foils produced by dimpling and ion milling. This revealed the existence of superlattice reflections and a crystal structure that is characteristic of the ordered B2 phase.

The as-forged alloy was direct-aged (DA) at 750 °C for 25 hours to stabilize the microstructure in a temperature regime close to the anticipated service temperature.[11] The microstructure of the resulting DA alloy is shown in Figure 1(b). No significant coarsening of the B2 phase was observed after direct aging at 750 °C for 25 hours. However, direct aging resulted in the formation of an acicular orthorhombic phase in the B2 matrix (Figure 1(b)). The structures of the B2 and orthorhombic phases were verified using electron diffraction analysis during TEM analysis. Typical electron diffraction patterns, obtained from three different zones, are presented in Figures 1(c) through (e) for the B2 and orthorhombic phases. Note that the extra weaker spots in the diffraction pattern correspond to the orthorhombic phase, which has also been detected in previous work by Fraser and co-workers.[7] Also, the brighter spots on the diffraction patterns confirm the ordered structure of the B2 phase.[7] The compositions of the individual phases in the DA microstructure were also determined (semiquantitatively) using energy-dispersive X-ray analysis during TEM analysis. This revealed that the actual composition of the orthorhombic phase was Nb-47Al-30Ti-1Mo, while the B2 phase had a composition of Nb-25.4Al-33.3Ti-1.7Mo (compositions quoted in at. pct.).

III. EXPERIMENTAL PROCEDURES

A. *Tensile Experiments*

Six smooth dog bone–shaped tensile specimens, with gage lengths of ~25.4 mm and thicknesses of ~3 mm, were fabricated using electrodischarge machining (EDM) techniques. The surfaces of the specimens were ground with emery paper to remove the few microns of the recast layer that were formed during EDM. The specimens were tested in the as-forged and DA (750 °C/25 h) conditions. The tensile tests were conducted under displacement control in accordance with the specifications of the ASTM E-8 code.[18] A servohydraulic testing machine was employed. The displacements across the gage sections were monitored continuously with a contact extensometer with a gage length of 25.4 mm. The tensile specimens were deformed continuously to failure at room temperature (25 °C) in laboratory air. A strain rate of 5×10^{-4} s^{-1} was used in the four tests (two sets of duplicate tests on the DA and as-forged material).

Incremental tensile tests were also performed on two smooth specimens that were ground with emery paper and polished with 6 and 1 μm diamond paste to remove the recast EDM surface layer. Colloidal silica was then used to remove the surface scratches during the final stages of polishing. After polishing, the polished surface of the gage section was etched in a solution of 25 pct HNO_3, 25 pct lactic acid, 25 pct H_2O_2, and 25 pct HF to reveal the underlying microstructure. The polished specimens were then used to study the tensile deformation mechanisms at room temperature. This was done by loading the specimens, in incremental stages, to stress levels that corresponded to fractions of the 0.2 pct offset yield strengths (YS) obtained from the first set of tensile tests (in which the test specimens were loaded continuously to failure). Following each incremental loading stage, the polished gage sections of the deformed specimens were examined under a light microscope. Deformation (slip bands) and fracture (microcracking) mechanisms were thus elucidated as functions of the applied stress.

B. *Fracture Toughness*

Fracture-toughness tests were performed on large single edge–notched (SEN) bend specimens ($25.4 \times 25.4 \times 114.3$ mm) in accordance with ASTM E-399 specifications.[13] The SEN samples were precracked under far-field compression loading at a stress intensity factor range of approximately 20 MPa$\sqrt{\text{m}}$ and a stress ratio ($R = K_{\text{min}}/K_{\text{max}}$) of 10. This resulted in precracks that were between 0.5 and 1 mm in length. The precracked SEN specimens were then loaded continuously to failure under three-point bend loading. A loading rate corresponding to a stress-intensity factor increase rate of 1 MPa$\sqrt{\text{m}} \cdot \text{s}^{-1}$ was used. Double edge–notched (DEN) samples[5] were also fabricated from the 44Ti alloy. These were also loaded to failure at a stress-intensity factor increase rate of 1 MPa$\sqrt{\text{m}} \cdot \text{s}^{-1}$ under four-point pure bend loading. Since the same nominal stresses and stress-intensity factors were applied to each notch, stable crack growth initiated from both notches. However, catastrophic failure typically only occurred from one of the notches, due to local microstructural differences in the crack-tip regions. The interactions of the second crack with the underlying microstructure were, thus, studied in the remaining halves of the specimens.

C. *Fatigue-Life Behavior*

Cyclic fatigue tests were conducted on cyindrical specimens with a gage length of 50 mm and a diameter of 12.7 mm. The fatigue-test specimens conformed to specifications in ASTM E-606[18] for constant stress amplitude–controlled cyclic fatigue tests. The fatigue tests were performed in a fully automated, closed-loop servohydraulic test machine. The stress amplitude–controlled tests were conducted at ambient temperature (~25 °C) at a constant cyclic frequency of 10 Hz (sinusoidal waveform) and a stress ratio ($R = \sigma_{\text{min}}/\sigma_{\text{max}}$) of 0.10. The first set of samples was loaded continuously to failure under cyclic loading. Subsequently, incremental fatigue tests were carried out on specimens that were loaded to various fractions of the measured number of cycles-to-failure obtained from the first set of stress amplitude–controlled tests. At each incremental loading stage, the cyclically deformed specimens were examined by scanning electron microscopy (SEM). The dominant deformation mechanisms were, thus, determined as functions of the number of cycles. The sequence of incremental loading and microscopic examination was continued until catastrophic failure occurred.

D. *Fatigue Crack Growth Behavior*

Fatigue crack growth behavior was studied using SEN specimens with the same dimensions as the fracture toughness specimens. However, the initial notch-to-width ratios of the fatigue specimens were ~0.25. As in the cyclic fatigue tests, a sinusoidal waveform was used in the fatigue crack growth experiments, which were carried out under load control in a servohydraulic testing machine. The SEN specimens were also precracked under three-point bend loading using similar precracking conditions to those that were employed for the precracking of the fracture-toughness specimens. Fatigue crack growth tests were also performed on compact tension (CT) specimens with a width (W) of 37.5 mm. The CT specimens of the 44Ti alloy were precracked using load-shedding techniques described subsequently.

After precracking, the fatigue crack growth experiments were carried out at a stress ratio ($R = K_{\text{min}}/K_{\text{max}}$) of 0.1 and a cyclic frequency of 10 Hz. Fatigue crack growth in all the specimens was monitored using a high-resolution (2.5 μm) telescope connected to a video monitoring unit. However, the fatigue crack growth tests were generally automated, and crack growth was also monitored *via* computer, using a direct current potential-drop technique. The automated tests were performed under load-shedding or load-increasing conditions, with controlled K gradients. The load-shedding or load-increasing rates were controlled using the following expression, prescribed by ASTM E647 code:[15]

$$K_{\text{max}} = K_{\text{max0}} \exp\left[C(a - a_0)\right] \qquad [1]$$

where K_{max} is the current stress intensity, K_{max0} is the initial stress intensity corresponding to a_0, a is the current crack length, a_0 is the initial crack length, and C is a constant that corresponds to the rate of load shedding. The fatigue-crack growth tests were started at stress intensity factor ranges (ΔK) of ~20 to 25 MPa$\sqrt{\text{m}}$. The specimens were then subjected to load shedding at a rate (C) of -0.08 mm^{-1} (-2 inch^{-1}). The fatigue threshold considered to correspond to a ΔK level at which no crack growth was detected (using

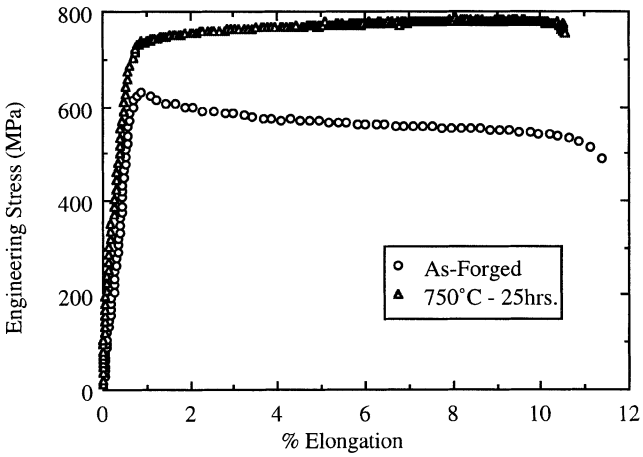

Fig. 2—Engineering stress–pct elongation curves for Nb-12A1-44Ti-1.5Mo at room temperature.

Table II. Tensile Properties of DA Nb-12Al-44Ti-1.5Mo at Room Temperature

Condition/ Heat Treatment	0.2 Pct Offset Yield Stress (MPa)	Ultimate Tensile Stress (MPa)	Total Elongation to Failure (Pct)
As-forged	628	—*	11.4
DA	733	783	10.5

* No ultimate tensile strength identified due to strain softening characteristics in this condition.

the direct current potential-drop technique) after $\sim 10^6$ cycles. The specimens were then subjected to load-increasing schemes with $C = +0.08\ \mathrm{mm}^{-1}$ ($+2\ \mathrm{inch}^{-1}$). The fatigue tests were stopped prior to specimen failure. The interactions of the cracks with the underlying microstructure were then studied using optical microscopy and SEM. Finally, the fracture modes in selected specimens were investigated using SEM, after loading the samples to failure under monotonic loading.

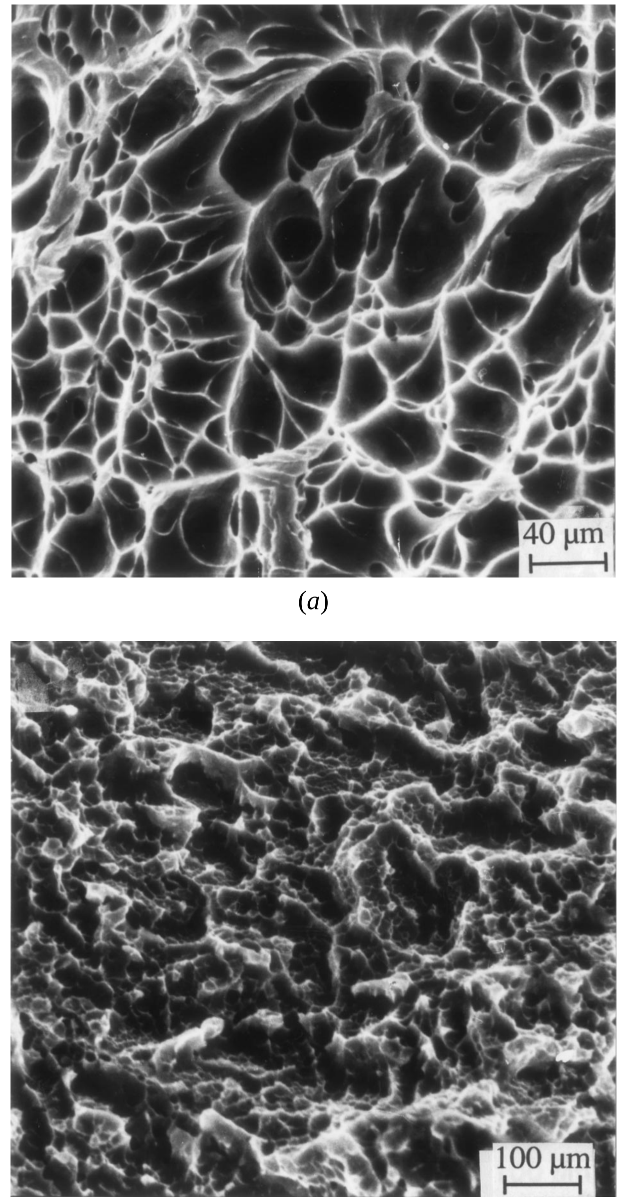

(*a*)

(*b*)

Fig. 3—Ductile dimpled fracture modes on the tensile fracture surface in Nb-12A1-44Ti-1.5Mo alloy: (*a*) as-forged and (*b*) direct-aged condition.

IV. RESULTS

A. *Tensile Fracture*

Plots of engineering stress *vs* total percentage elongation are shown in Figure 2 for the as-forged and DA conditions. Note that the 44Ti alloy exhibits essentially elastic–perfectly plastic behavior in both conditions. However, the as-forged alloy exhibits strain softening during plastic deformation under tensile loading (Figure 2). Reasons for the strain-softening behavior are unknown at present. However, the necking (localized deformation) associated with the strain softening resulted in a percentage reduction of area of 40 pct in the as-forged condition and a corresponding value of 10 pct in the DA condition.

The uniaxial tensile properties obtained in the as-forged and heat-treated conditions are summarized in Table II. The 44Ti alloy exhibited attractive combinations of tensile strength and ductility in the as-forged and DA conditions. The alloy also exhibits a plastic elongation-to-failure (ε_p) of approximately 11 pct in these conditions. Furthermore, tensile fracture in the as-forged and DA conditions occurred by ductile dimpled fracture (Figure 3), which is not normally observed in ordered intermetallic materials at room temperature.

The incremental tensile tests performed on the DA alloy revealed clear evidence of slip-band formation after loading to approximately 9.6 pct of the 0.2 pct offset YS (Figure 4(a)). The localized slip bands spread gradually across the gage section of the test specimen, as the applied stress increased to 70 pct of the 0.2 pct offset YS (Figure 4(b)). Intense slip-band activity, coupled with intersection of the slip bands, was observed at a stress level of 83.7 pct of the 0.2 pct offset YS (Figure 4(c)). This was followed by roughening of the specimen surface and the crack initiation from coarsening slip bands at ~97.5 pct of the 0.2 pct offset YS (Figure 4(d)). Multiple microscopic cracks were observed to initiate in this manner. However, only one of

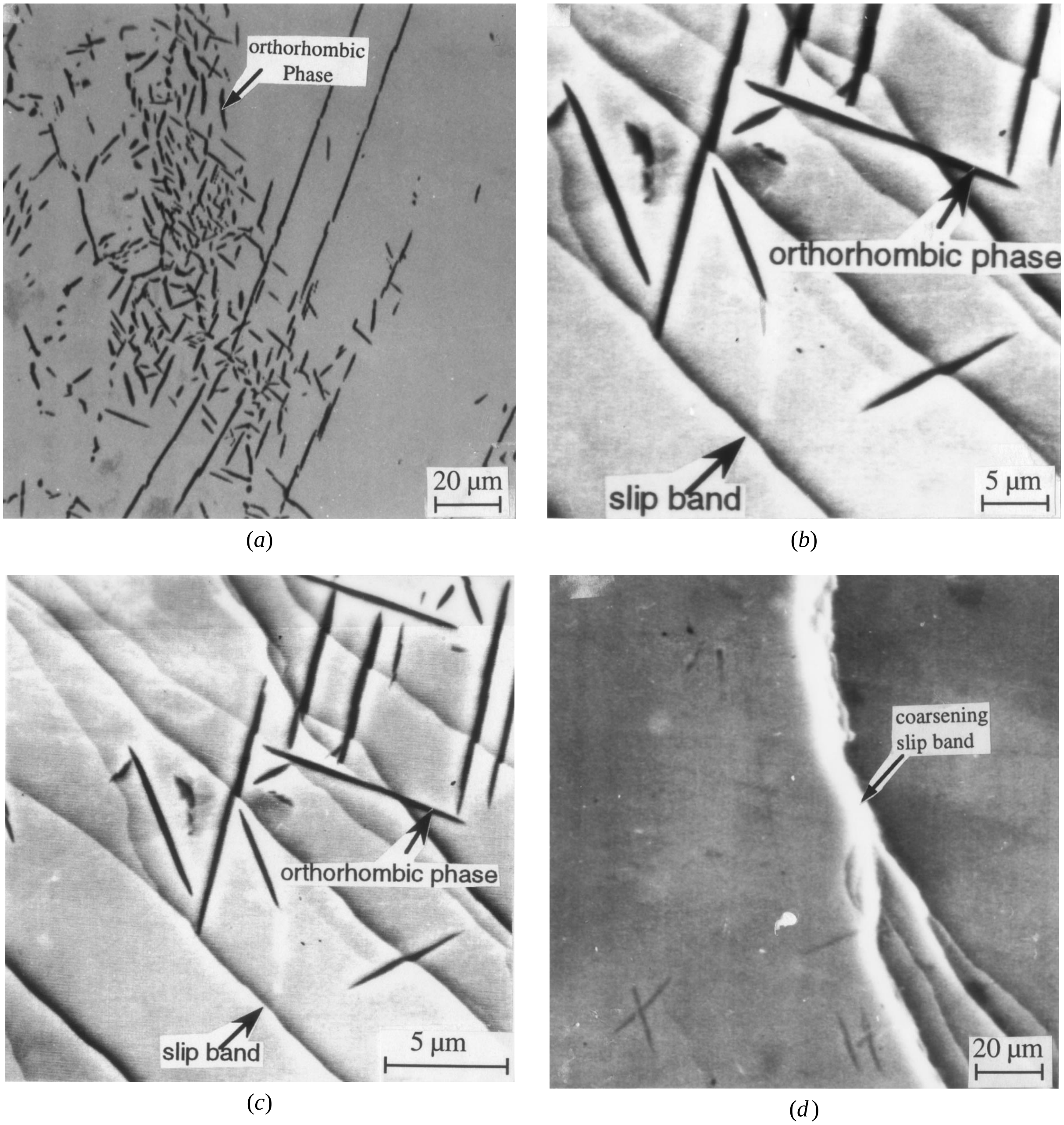

Fig. 4—Scanning electron micrographs showing deformation and cracking mechanisms in the uniaxially deformed specimen: (*a*) 9.6 pct YS, (*b*) 70 pct YS, (*c*) 83.7 pct YS, and (*d*) 97.5 pct YS. YS = yield stress.

the initiated cracks extended into the bulk of the specimen, culminating in catastrophic failure at a stress level of 915 MPa.

B. *Fracture Toughness*

The measured fracture toughness (K_Q) was 92 MPa $\sqrt{m}$ in the L-T orientation and 60 MPa $\sqrt{m}$ in the T-L orientation. Since the ASTM E-399 code[18] requires that the specimen thickness satisfy the condition that the specimen thickness (B) be greater than or equal to the term $r = 2.5\ (K_Q/\sigma_{ys})^2$, the value of r was determined for the T-L and L-T orientations (where K_Q is the stress-intensity factor at the fracture load and σ_{ys} is the yield strength). For the DA condition, r was determined to be 0.0168 m in the T-L orientation. Since the specimen thickness was 0.0254 m, the fracture toughness of 60 MPa $\sqrt{m}$ in the T-L orientation satisfies the ASTM E-399 code. Hence, the fracture toughness obtained in the T-L orientation corresponds to a K_{Ic} value. However, the fracture toughness of 92 MPa$\sqrt{m}$ obtained in the L-T orientation corresponds only a thickness-dependent K_Q value, since the ratio is 0.0394 m, which is greater than the specimen thickness.

In any case, the fracture toughness was higher when the cracks intercepted a larger number of grain boundaries per unit volume, *i.e.*, in the L-T orientation. The high toughness values (60 to 92 MPa$\sqrt{m}$) are also consistent with the results obtained from the experiments on DEN specimens. The latter revealed wavy slip traces that correspond to the stress field ahead of a blunt notch,[19] as shown in Figure 5(a). Multiple

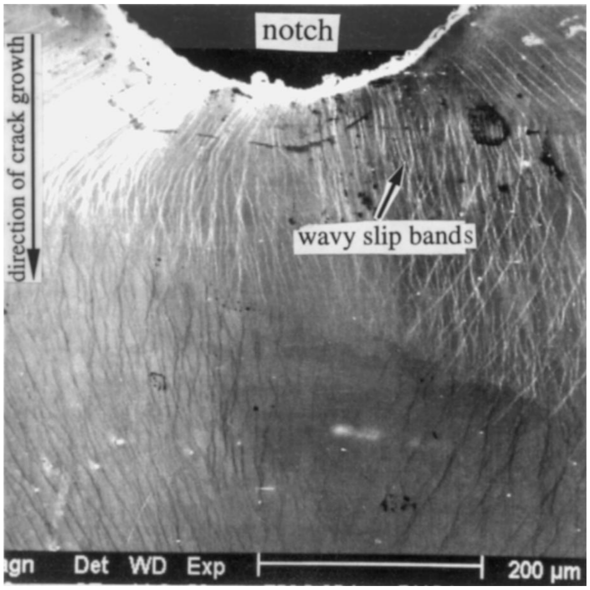

(*a*)

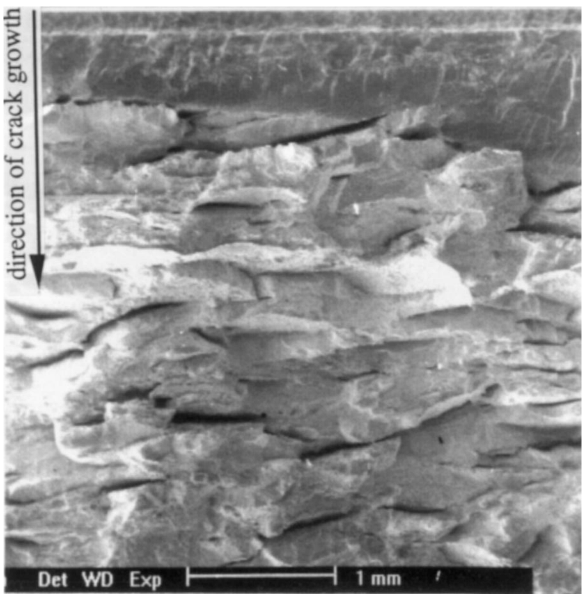

(*b*)

Fig. 5—Typical fracture mechanisms in Nb-12A1-44Ti-1.5Mo alloy: (*a*) slip bands ahead of notch; and (*b*) ductile dimpled fracture and secondary splitting along grain boundary.

intergranular splits/cracks were also observed to form in the direction perpendicular to the main crack growth direction (Figure 5(b)).

It is of interest to comment on the implications of wavy slip bands in the DA alloy (Figure 5(a)). These indicate that the very high fracture toughness in the DA condition is due partly to the effects of crack-tip plasticity. This is consistent with the plots of engineering stress *vs* total elongation percentage, which show clear evidence of plasticity (ductility of ~10.5 pct) and a 0.2 pct offset YS of ~733 MPa in the DA condition. The relatively high fracture toughness of the 44Ti alloy is, therefore, associated with the significant levels of crack-tip plasticity.

Similar improvements in fracture toughness have been observed in the Nb-15Al-40Ti (40 to 110 MPa$\sqrt{m}$)[1,2] and

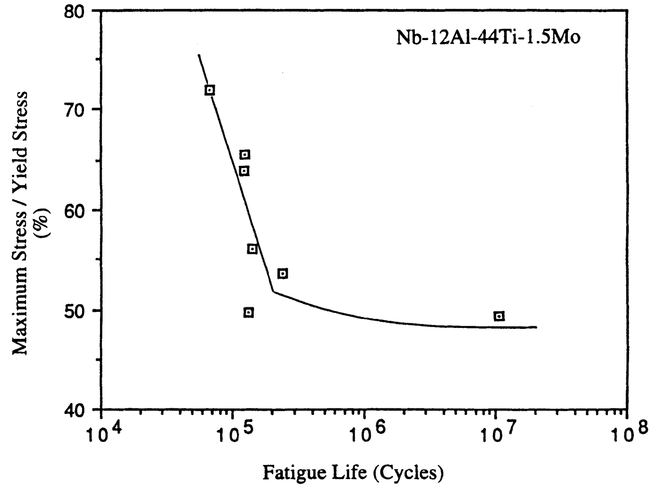

Fig. 6—Variation of cyclic stress amplitude ($\Delta\sigma/2$) with fatigue life (N_f).

Nb-13Cr-37Ti (60 to 85 MPa$\sqrt{m}$)[16,17] alloys with B2 and bcc structures, respectively. As in this study, the high fracture toughness levels in these alloys were associated with Ti levels that were close to ~40 at. pct. The high fracture toughness levels were also associated with the onset of significant levels of crack-tip plasticity.

Finally, in this section, it is interesting to note that the onset of crack-tip plasticity in a similar Nb-15Al-40Ti alloy was predicted by Farkas[10] in recent atomistic simulations using a method of molecular statics (embedded-atom method). This suggests that more-complex (quaternary/quinternary) alloy compositions may be designed by using atomistic simulations to determine whether crack-tip plasticity is likely to occur before cleavage fracture. Such simulations could significantly reduce the cost and time required for further "optimization" of niobium aluminide–based alloy compositions.

C. *Fatigue-Life Behavior*

As discussed earlier, fatigue tests were conducted on dog bone–shaped specimens in accordance with ASTM E-606 specifications.[18] The stress–fatigue life curve obtained in the DA condition is presented in Figure 6. Due to the limited amount of available material and the relatively large specimen sizes, only a limited number of fatigue-life tests were conducted, as shown in Figure 6. This shows the variation of cyclic stress amplitude with the number of cycles to failure (N_f). An estimate of the endurance limit was obtained for the DA 40Ti alloy using the limited available data. The endurance limit (corresponding to the cyclic stress range at which the fatigue life is ~10^7 cycles) for the DA alloy was estimated to be ~420 MPa, *i.e.*, approximately half of the ultimate strength. The stress-life behavior is, therefore, similar to that of steels in which the endurance limit is typically close to half of the ultimate tensile strength.

Crack initiation in incremental stress amplitude–controlled fatigue tests was associated with slip-band initiation and slip-band interactions/intersections. This is shown in Figures 7(a) through (f) for a test specimen that was deformed under cyclic loading at a maximum stress of 0.67 σ_{ys} (where σ_{ys} is the 0.2 pct YS in uniaxial

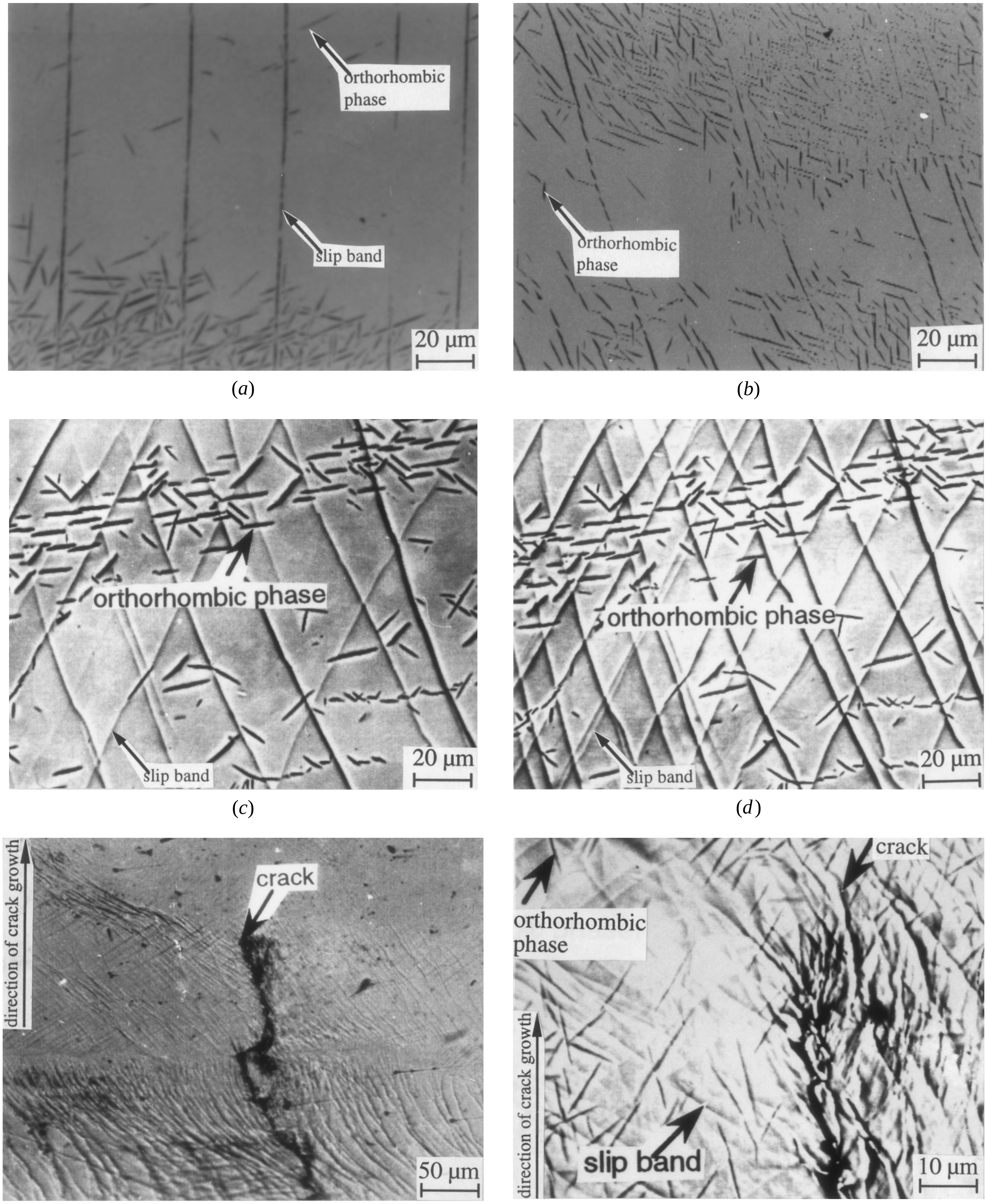

Fig. 7—Scanning electron micrographs of the cyclically deformed stress amplitude–controlled specimen of the intermetallic after (*a*) 1 cycle, (*b*) 10 cycles, (*c*) 100 cycles, and (*d*) 10,000 cycles and after 40,000 cycles of loading; (*e*) optical micrograph and (*f*) scanning electron micrograph. Total fatigue life of the test specimen was 45,430 cycles.

tension). Slip-band initiation occurred after the very first fatigue cycle (Figure 7(a)). This was not surprising, since the applied stress levels in the very first fatigue cycle were generally in excess of the stress at which slip-band initiation was observed in the incremental tensile tests, *i.e.*, the applied cyclic stresses were generally greater than 9.6 pct of the 0.2 pct YS (Figure 4(a)). Furthermore, the density of slip bands was observed to be greater after 10 cycles of fatigue loading (Figure 7(b)). Evidence of slip-band intersection became clearly apparent after 100 cycles of fatigue loading (Figure 7(c)), and localized slip (slip bands) spread gradually across the entire gage section, as the specimen was cyclically deformed for ~10,000 cycles (Figure 7(d)).

The transition from localized inhomogeneous plastic deformation to bulk homogeneous plastic deformation was complete after 30,000 cycles. Very intense surface roughening was apparent in the gage sections of the incrementally deformed specimens prior to the onset of catastrophic failure (Figures 7(e) and (f)). This facilitated crack nucleation, which occurred as a result of the coarsening of slip bands that were formed on the surface of the specimen after 40,000 cycles (Figure 7(e)). The initiated fatigue cracks propagated by crack openings along the intersecting slip bands that were induced in regions of high local stress concentration ahead of the tip of the dominant crack (Figure 7(f)). Final failure occurred after 45,430 cycles by a ductile dimpled fracture mode that was similar to that observed under monotonic loading (Figure 3).

The TEM analysis of the deformed gage sections of the fatigue-life specimens was also carried out on a specimen that was deformed continuously to failure at a stress range ($\Delta\sigma$) of 296 MPa. The TEM analysis of the deformation surface revealed the existence of dislocations between slip bands (Figure 8(a)). Higher-magnification TEM imaging showed a network of dislocations in between the slip bands (Figure 8(b)). In contrast, no slip bands were observed in the TEM analysis of foils that were taken from the bulk regions (Figure 8(c)). Instead, the deformation in this region was associated with well-defined Taylor lattices that are indicative of limited dislocation mobility. Pairs of partial dislocations were also observed in the regions adjacent to the Taylor lattices (Figure 8(d)).

The fracture surfaces of the fatigue-life specimen provided some useful insights into the mechanisms of fatigue crack initiation and growth. Room-temperature fatigue fracture surfaces of the alloy deformed at a maximum cyclic stress of 483 MPa (70 ksi, N_f = 143,851 cycles), revealed distinct regions of early microscopic crack growth and overload failure (Figure 9(a)). Microscopic cracks were evident adjacent to the region of crack initiation and in the region of stable crack growth (Figures 9(a) and 9(b)). The sample cyclically deformed at a higher stress of 552 MPa (80 ksi, N_f = 122,347 cycles) contained a small, yet distinct, region of stable crack growth (Figure 9(c)). High-magnification SEM observation of the region of stable crack growth revealed evidence of fatigue striations (Figure 9(c)). Final fracture occurred by ductile dimpled fracture, with some incidence of secondary cracking (Figure 9(d)).

D. *Fatigue Crack Growth and Threshold Behavior at 25 °C*

The room-temperature fatigue crack growth rates in the alloys studied are compared to those of mill annealed Ti-6Al-4V, [20] IN718, [21] and pure Nb[22] in Figure 10(a). The room-temperature fatigue crack growth rates in the 44Ti alloy are comparable to those in mill annealed Ti-6Al-4V with an equiaxed microstructure.[20] However, the fatigue crack growth rates are faster than those in a beta heat-treated Ti-6Al-4V alloy with a Widmanstatten microstructure[20] (Figure 10(a). Similarly, the fatigue crack growth rates are somewhat faster than those in IN 718[21] and pure Nb.[22] The room-temperature fatigue crack growth rates in the 44Ti alloy were also comparable in the T-L and L-T orientations (Figure 10(b)).

At 750 °C, the near-threshold fatigue crack growth rates in the 44Ti alloy were generally slower than those at room temperature (Figure 10(c)). The slower near-threshold fatigue growth rates at 750 °C were associated with the effects of a thick rutile (TiO_2) oxide scale that formed during elevated-temperature testing (Figure 11(a)). This suggests that oxide-induced crack closure occurred in the near-threshold regime, where the crack opening displacements were comparable to the oxide thickness.[23] Quantitative estimates of the closure stress-intensity factor (K_{cl}) may be estimated from a modified Dugdale–Barenblatt closure model.[23] The model accounts for the wedging induced by the oxide layer behind the crack tip, as shown schematically in Figure 11(b). The Dugdale–Barenblatt model yields the following expression for the closure stress–intensity factor:

$$K_{cl} = \frac{dE}{4(\pi l)^{1/2}(1 - \mu^2)} \qquad [2]$$

where d is the excess oxide thickness, $2l$ is the wedge length of the oxide film, μ is the Poisson's ratio, and E is the Young's modulus.

Since the oxide completely filled the crack (Figure 11(a)), $2l$ in Eq. [2] (Figure 11(b)) was assumed to be equal to the distance from the crack tip to the notch tip, *i.e.* 1.4 mm, at a ΔK of 12.1 MPa$\sqrt{m}$ and a total crack length of 7.75 mm. An excess oxide thickness, $d = 10$ μm, was determined for the 44Ti alloy under the same conditions. Using a Young's modulus value obtained from a plot of stress *vs* strain (E = 120 GPa) and assuming $\nu = 0.3$ yields a K_{cl} (from Eq. [3]) value of ~7.0 MPa$\sqrt{m}$ at 750 °C. Hence, the effective stress intensity–factor range ($\Delta K_{eff} = K_{max} - K_{cl}$) was determined to be ~5.1 MPa$\sqrt{m}$ when the test was stopped at ΔK = 12.1 MPa$\sqrt{m}$. This is close to the measured room-temperature fatigue threshold (note that the fatigue threshold was taken to correspond to a stress intensity–factor range at which no crack growth was detected after ~10^6 cycles) obtained for the DA alloy (~4.5 MPa$\sqrt{m}$). The slower crack growth rates obtained at 750 °C are, therefore, attributed largely to the effects of oxide-induced crack closure.

Consistent with the previous arguments, much faster fatigue crack growth rates were obtained in the mid- and high-ΔK regimes where the crack opening displacements exceeded the excess oxide thicknesses. In fact, the fatigue crack growth rates in the mid- and high-ΔK levels (11 to 30 MPa$\sqrt{m}$) were up to 1000 times faster in the 44Ti alloy at 750 °C, when the cracked specimens were cyclically loaded at room temperature (where no thick oxide scales were formed) prior to fatigue crack growth testing at 750 °C (Figure 10(c)). Note that the data were obtained from ΔK-increasing tests, with no oxide scale initially wedging open the crack. The faster growth rates are attributed to the

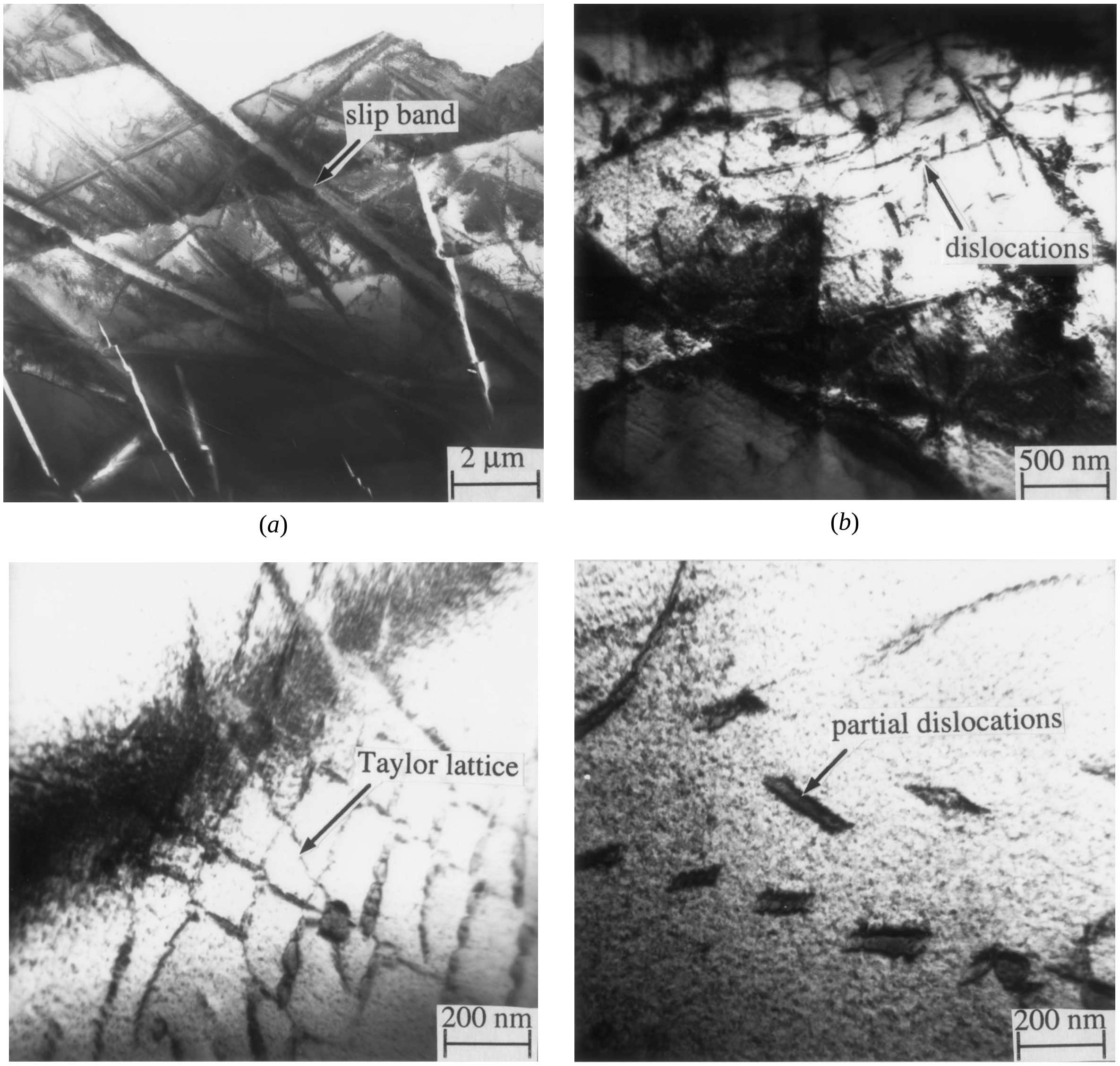

(*a*) (*b*) (*c*) (*d*)

Fig. 8—TEM photomicrographs of the deformed gage section of smooth fatigue life specimen that was deformed continuously to failure at a stress range of 296 MPa: (*a*) dislocations in between slip bands at surface; (*b*) higher magnification image showing dislocations between slip bands; (*c*) Taylor lattices in the bulk of the specimen, and (*d*) pairs of partial dislocations adjacent to Taylor lattice.

inadequate time for oxide formation (within the crack) at these faster growth rates. Furthermore, oxide-induced crack closure is unlikely to occur at high ΔK levels, since the crack opening displacements far exceed the measured excess oxide thicknesses in this regime.

Finally, in this section, it is important to discuss the fatigue fracture modes. At room temperature, a faceted crack growth mode was observed in the near-threshold regime (Figure 12(a)), while fatigue striations were apparent on the fracture surfaces in the mid- and high-ΔK regimes (Figure 12(b)). The fracture modes at 750 °C were also similar to those observed at room temperature. Fatigue striations and faceted fracture modes were observed on the fracture surfaces of the specimens that were tested at 750 °C at a ΔK of ~20 MPa$\sqrt{\text{m}}$ (Figure 12(a)). However, secondary cracking was also observed at higher ΔK levels (~30 MPa$\sqrt{\text{m}}$), as shown in Figure 12(b). The fatigue fracture modes in the 44Ti alloy were, therefore, similar to those in ductile metals and their alloys.[24]

V. DISCUSSION

A. *Microplasticity*

The results obtained in this study suggest that localized plasticity is induced in the 44Ti alloy (Figures 4(a) through (d)) at stress levels that are considerably below the bulk yield stress. Similar evidence of microplasticity has been observed in earlier studies on the metastable β Ti-15V-3Cr-3Al-3Sn alloy.[25] The initially localized plasticity is distributed randomly, presumably within favorably oriented grains. However, the localized microplasticity spreads gradually across the gage sections of the specimen, as the stress increases under uniaxial tensile loading. The distribution of

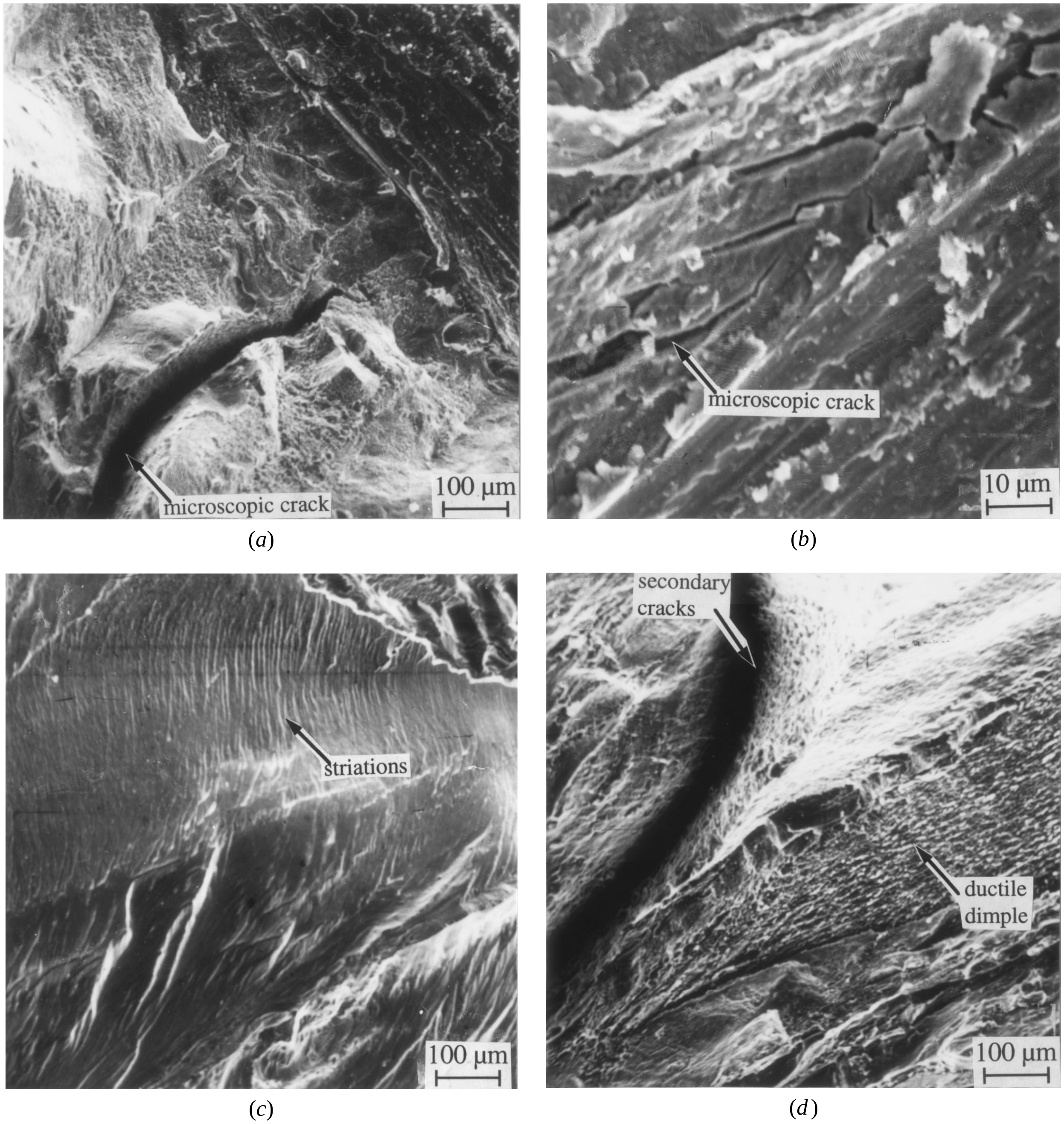

Fig. 9—Cyclic fracture modes: (*a*) region of crack initiation/early crack growth, (*b*) microscopic cracks, (*c*) region of early crack growth, and (*d*) overload region.

microplasticity is attributed to the combined effects of grain orientation, elastic anisotropy or constraint and the resultant stress concentration effects due to contributions from grain shape, grain-boundary triple junctions, and inherent surface defects associated with electrodischarge machining procedures.

It is also important to note here that the nonlinearities associated with localized yielding cannot be detected accurately using "standard" extensometers, which have a strain resolution of 10^{-4}. Instead, the detection of localized microplasticity requires the use of microscopic techniques that can reveal the distribution of slip bands or other slip characteristics within individual grains that are favorably oriented for slip and shear localization. Furthermore, the grain boundaries of the B2 and/or orthorhombic phases may provide the necessary sites for dislocation pileup to occur prior to the onset of shear localization phenomena. Such localized pileup phenomena may contribute to the formation of the observed slip bands in the so-called linear elastic regime, where band stretching/distortion is generally thought to control the deformation characteristics. It is also evident, from the preceding discussion, that microplasticity will spread as the resolved shear stress levels in individual grains increase to levels that are sufficient to promote dislocation

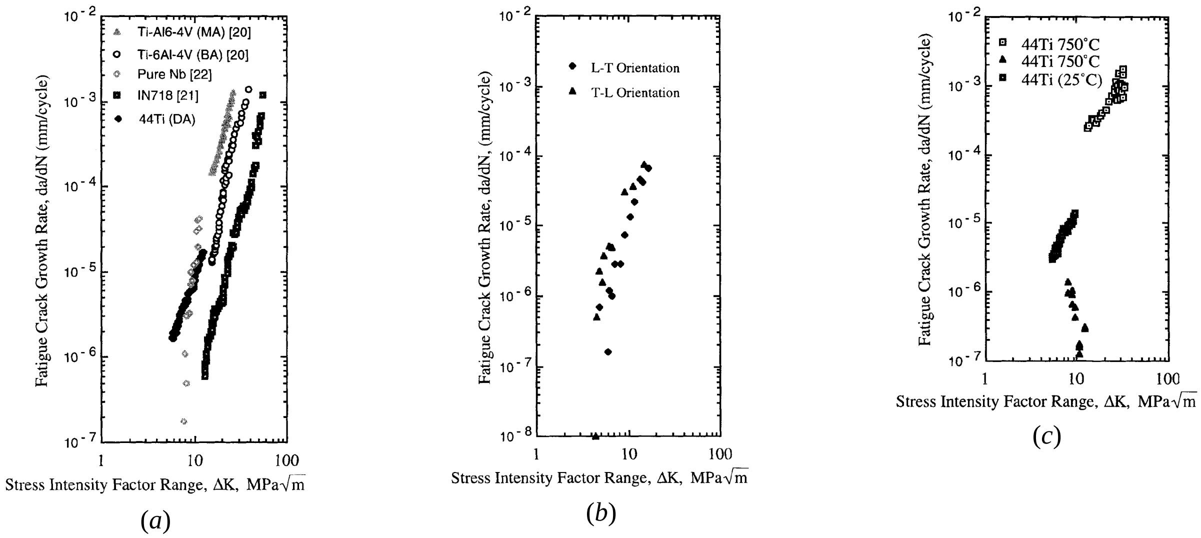

Fig. 10—Summary of fatigue crack growth rates of Nb-12A1-44Ti-1.5Mo alloy (*a*) compared with Ti-6A1-4V,[20] Nb,[22] and In718,[21] (*b*) orientation effects and (*c*) at 750 °C.

motion completely across the gage sections of the tensile specimens. The onset of bulk yielding appears to correspond to the latter condition.

B. *Microplasticity and Fatigue*

The observation of microplasticity during incremental uniaxial deformation provides a viable explanation for the occurrence of forward plasticity during cyclic loading of smooth specimens at stress levels that are considerably below the bulk yield stress. As discussed earlier, such microplasticity may initiate at imperfections in the microstructure. Since the forward plastic strain tends to accumulate during the rising portion of the fatigue cycle, and the reversed plastic strains accumulate during load reversal, the microplastic strains accumulated during cyclic loading should be considerably greater than the strains that develop under equivalent monotonic loading conditions.

Consequently, the initiation of macroscopic cracks in smooth specimens occurs at stress levels that are considerably below the bulk yield stress. This occurs when the accumulated strains are sufficient to initiate and propagate damage due to the microplasticity and/or microcracking. Conversely, crack initiation will not occur when the accumulated microplastic strains are not sufficient to nucleate microscopic cracks. This provides an appealing rationale for the occurrence of an endurance limit in some materials, such as the 44Ti intermetallic alloy that was examined in this study. It is also possible that the relative ease of microplasticity may be used to explain the apparent absence of a well-defined endurance limit in fcc materials.[24] However, further work is required to verify such speculation.

Nevertheless, considering the rising portion of the first cycle of fatigue loading, it is possible to understand why microplasticity is important for subsequent cyclic plasticity phenomena. During the forward portion of the first fatigue cycle, localized microplasticity is evident through the occurrence of stress-induced slip-band formation. The slip bands form, after the very first fatigue cycle, in grains that are favorably oriented for slip and/or shear localization (Figure 7(a)). Progressive accumulation of damage in the initial microplastic sites, coupled with the nucleation of slip-band activity on other favorably oriented grains, culminates in the nucleation of one or more microscopic cracks (Figures 7(a) through (f)). The combined effect of strain concentration and slip band/environmental interactions is greatest at corners on the surface of the test specimen. These corners, therefore, provide the most-likely sites for the initiation of fatigue cracks.

The precise transition from a slip band to a microscopic crack is difficult to characterize exactly (Figures 7(a) through (e)). Nevertheless, it is apparent from the current results that the fine microscopic cracks are nucleated by the gradual coarsening of the slip bands during repeated cyclic stressing (Figures 7(a) through (f)). The observed crack nucleation mechanism is somewhat similar to that suggested in an earlier work by Neumann.[26] In the Neumann model, [26] alternating slip results in the nucleation of slip bands in grains both at and beneath the surface. The formation of slip bands, coupled with resultant sliding along these bands, results in the formation of slip steps. Subsequent kinematic irreversibility, arising from the combined effects of partially reversible slip and material/environmental interactions, results in the nucleation of fatigue cracks.

C. *Fatigue Crack Growth*

It is of interest to discuss the room-temperature fatigue crack growth behavior that was observed in the 44Ti alloy. First, it is encouraging to note that the fatigue crack growth rates were close to those in IN718,[21] pure Nb,[22] and mill annealed and beta annealed Ti-6Al-4V.[20] The Paris exponents, determined from the slope of the da/dN *vs* ΔK plots in the mid-ΔK regime, were between ~2.5 and 4.1 at room temperature. The Paris exponents of the 44Ti alloy were, therefore, close to those of ductile metals and their alloys (Table III). Furthermore, the effects of forging orientation on fatigue crack growth were relatively small (Figure 10(b)).

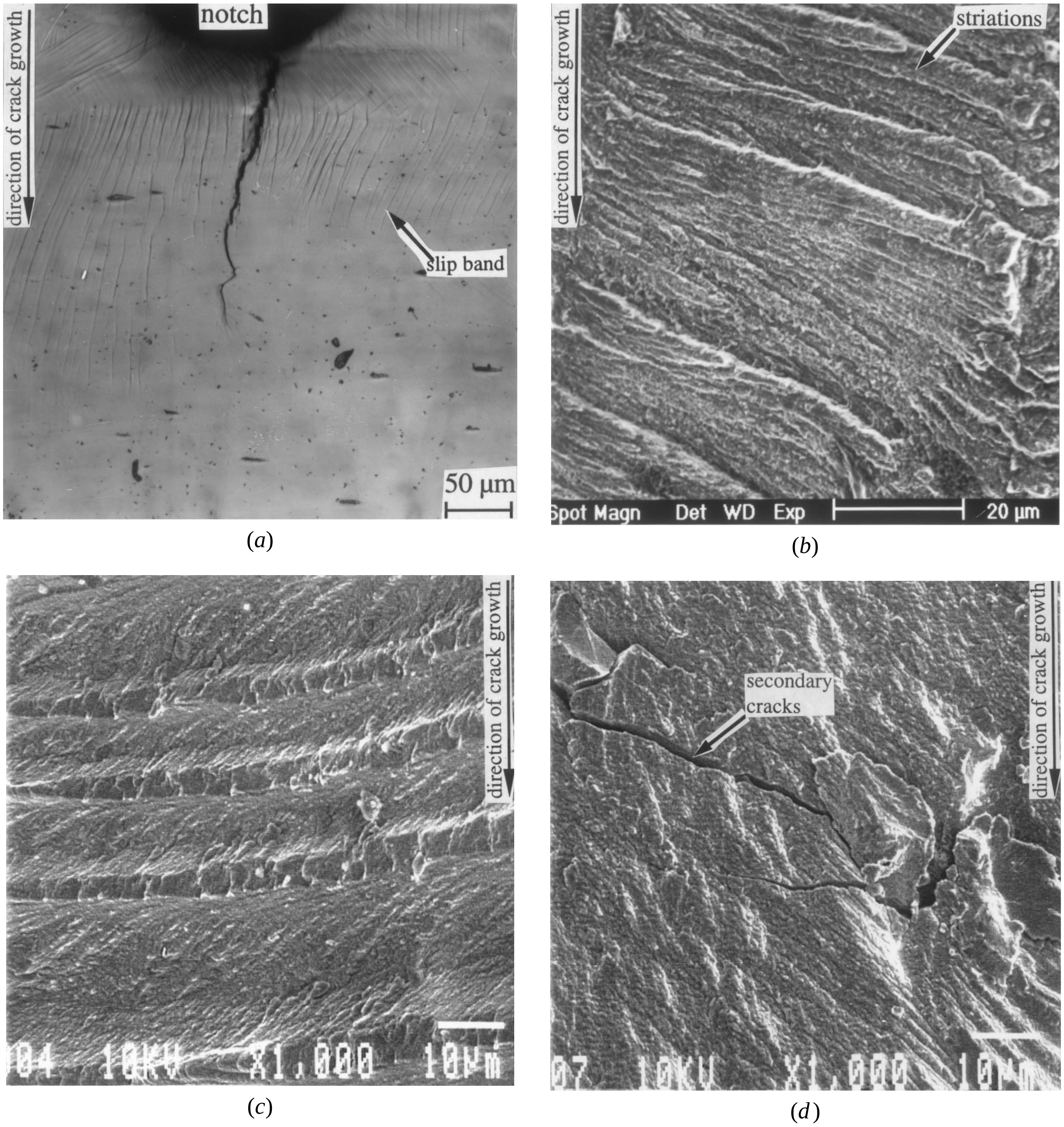

Fig. 11—Typical fatigue fracture mode in Nb-12A1-44Ti-1.5Mo alloy at room-temperature: (*a*) slip band formation ahead of crack tip; (*b*) fatigue striations in mid-ΔK regime, at 750 °C; (*c*) striations and faceted fracture in the 44Ti alloy at a ΔK of ~20 MPa$\sqrt{m}$; and (*d*) secondary cracking at ΔK ~30 MPa$\sqrt{m}$ in 44Ti alloy.

The 44Ti forging was, therefore, resistant to fatigue crack growth in the T-L and L-T orientations.

The crack profiles indicate that fatigue crack growth in the 44Ti alloy occurs by the "unzipping" of the microscopic cracks along alternating slip bands (Figures 7(e) and (f)). The unzipping crack growth mechanism is similar to that reported by Neumann[26] and Liu[27] for crack growth in single crystals. Similar observations of crack growth by unzipping have been reported by Dubey *et al.*[28] in a recent study of a polycrystalline, equiaxed $\alpha + \beta$ Ti-6Al-4V alloy. The unzipping crack growth mechanism, proposed in these earlier studies, is, therefore, applicable to the polycrystalline Nb-12Al-44Ti-1.5Mo intermetallic alloy, in which the alternating slip bands form, presumably, as a result of shear localization phenomena.

At an elevated temperature (750 °C), fatigue crack growth in the near-threshold regime was significantly affected by oxide-induced crack closure. Evidence of oxide-induced crack closure is presented in Figure 12(a). This shows a side profile of a fatigue crack growth specimen that was tested at 750 °C. The side profile shows clear evidence of a thick layer of TiO_2 (rutile) that fills the gap between the crack faces (Figure 12(a)). Since the excess thickness of TiO_2 is sufficient to wedge open the cracks during fatigue crack

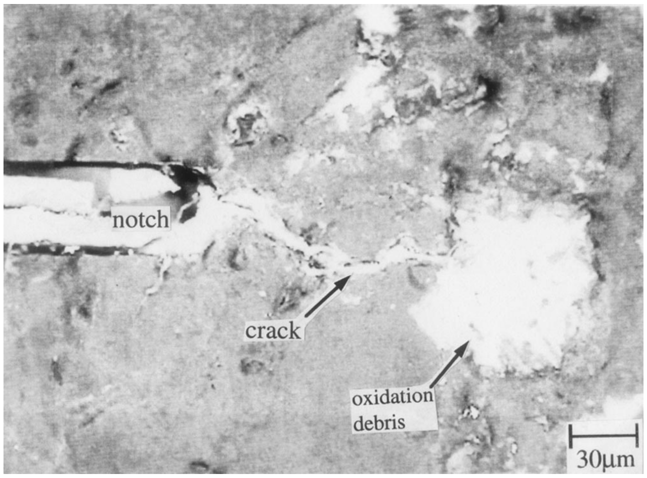

(*a*)

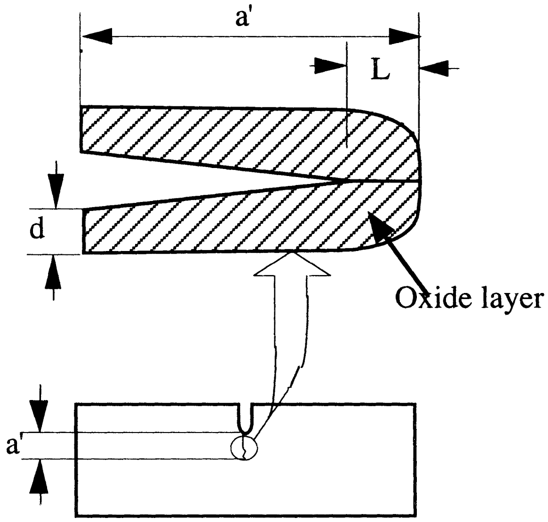

(*b*)

Fig. 12—(*a*) Optical micrograph of the side of 44Ti specimen following fatigue crack growth test at 750 °C. (*b*) Schematic illustration of the mechanism of oxide-induced closure.

Table III. Summary of Fatigue Crack Growth Constants

Nominal Alloy Compositions (At. Pct)	Paris Exponent (m)	Paris Coefficient A (mm/cycle $(MPa\sqrt{m})^{-m}$)	ΔK_{th} ($MPa\sqrt{m}$)
44Ti (DA)	2.5	5×10^{-8}	4.6
Ti-6Al-4V (mill annealed)[20]	4.1	1.8×10^{-9}	—*
Ti-6Al-4V (beta annealed)[20]	5.5	5.1×10^{-12}	—*
Pure Nb [22]	11.4	4.8×10^{-17}	7.8
IN718 [21]	4.4	1.2×10^{-11}	12.7

* Fatigue threshold data not available in Ref. 20.

growth at elevated temperatures (Figure 12(b)), the slower fatigue crack growth rates (compared to those obtained at room temperature) are attributed largely to the effects of oxide-induced crack closure.

Further proof of the role of oxide-induced closure at 750 °C was obtained by performing the following experiment. First, an SEN bend specimen was subjected to fatigue crack growth testing at 750 °C in laboratory air. The same specimen was then cyclically loaded in laboratory at 25 °C to further extend the crack in the absence of thick thermally induced oxides. (Note that it is recognized that monolayers of oxides may form during room-temperature fatigue, but such thin nanoscale layers are generally not sufficient to induce oxide-induced crack closure in the alloy examined in this study.) Finally, fatigue crack growth is continued at 750 °C in air in an effort to observe the crack growth behavior in the absence of thermally-induced oxide layers at the crack tip.

The results obtained from the previous experiment are presented in Figure 10(c). Note the slower fatigue crack growth rates that occur during the first loading sequence, in which the specimen was cyclically deformed at 750 °C. The slower fatigue crack growth rates are attributed to the effects of oxide-induced crack closure. Furthermore, the fatigue growth rates were up to 1000 times faster after subsequent precracking at room temperature (where thick thermally induced oxides do not form) and testing at 750 °C. Hence, the fatigue crack growth rates are much faster in the absence of thick crack-tip oxide layers that cause oxide-induced crack closure to occur at 750 °C (Figures 12(a) and (b)).

VI. CONCLUSIONS

1. The 44Ti alloy has an attractive combination of room-temperature ductility and tensile strength in the as-forged and DA conditions. During monotonic loading, localized microplasticity occurs by slip-band formation at stress levels as low as 9.6 pct of the bulk yield stress. Subsequent proceeds by the gradual spread of microplasticity (slip bands) across the gage section until bulk yielding occurs. The onset of bulk yielding is associated with the spread of slip bands completely across the gage section. Subsequent bulk plastic deformation results in intense surface roughening and microcrack nucleation, prior to the onset of catastrophic failure under monotonic loading.
2. The nucleation of fine microscopic cracks (in smooth specimens) during fatigue loading is attributed to the accumulation of microplasticity in regions of high stress concentrations and, presumably, in favorably oriented grains. Crack initiation also occurs by the coarsening of slip bands. However, the precise condition for the onset of microscopic crack initiation is difficult to determine exactly, due to the gradual nature of the transition from a coarse slip band to a microcrack.
3. Ductile dimpled tear regions (similar to those in metallic materials) are observed on the fracture surfaces of smooth and notched specimens deformed to failure under monotonic loading in the as-forged and DA conditions. The DA alloy has a thickness-dependent fracture toughness of 92 $MPa\sqrt{m}$ in the L-T orientation, compared to a thickness-independent fracture toughness of 60 $MPa\sqrt{m}$ in the T-L orientation. The fracture toughness is, therefore, greater when the direction of crack growth is perpendicular to the elongated forged grains. The high fracture-toughness levels are attributed largely to the effects of crack-tip plasticity.
4. Fatigue crack nucleation occurs by the coarsening of slip bands that form at the surface. Subsequently, fatigue crack

growth occurs by an unzipping crack growth mechanism similar to that postulated by Neumann[26] and Liu.[27] This gives rise to a faceted crack growth mechanism. However, secondary cracking is also observed, in addition to the faceted crack growth mode, at high ΔK levels, where striations are also observed.

5. Fatigue crack growth rates in the 44Ti alloys are comparable to those in mill annealed and beta annealed Ti-6Al-4V, IN718 and pure Nb at room temperature. The 44Ti alloy also has better fatigue crack growth resistance when the direction of fatigue crack growth is oriented perpendicular to elongated grains produced *via* forging. Slower fatigue crack growth rates at 750 °C are due largely to the effects of crack-tip shielding due to oxide-induced closure.

ACKNOWLEDGMENTS

The research was completed with the support of a grant from the Office of Naval Research (Grant No. N00014-94-1-0501). The authors are grateful to the Program Monitor, Dr. George Yoder, for his encouragement and support. Appreciation is extended to Mr. Andrew Culbertson for providing additional financial support from the Naval Air Warfare Center. The authors also thank General Electric Aircraft Engines for providing the forged material that was used in this study.

REFERENCES

1. F. Ye, C. Mercer, and W.O. Soboyejo: *Metall. Mater. Trans. A*, 1998, vol. 29A, pp. 2361-74.
2. J. DiPasquale, D. Gahutu, D. Konitzer, and W.O. Soboyejo: in *High Temperature Ordered Intermetallic Materials VI*, J.A. Horton, S. Hanada, I. Baker, R.D. Noebe, and D.S. Schwartz, eds., Materials Research Society, Pittsburgh, PA, 1994, pp. 1347-52.
3. T.S. Srivatsan, J. DiPasquale, W.O. Soboyejo, and D.G. Konitzer: *Eng. Fract. Mech.*, 1997, vol. 561 (3), pp. 293-310.
4. T.S. Srivatsan, J. DiPasquale, and W.O. Soboyejo: in *Deformation and Fracture of Ordered Intermetallic Materials III*, W.O. Soboyejo, T.S. Srivatsan, and H.L. Fraser, eds., TMS, Warrendale, PA, 1996, pp. 483-506.
5. T.S. Srivatsan, S. Sriram, C. Daniels, K. Dhana Singh, W.O. Soboyejo, and D. Konitzer: in *Fatigue and Fracture of Ordered Intermetallic Materials II*, W.O. Soboyejo and T.S. Srivatsan, eds., TMS, Warrendale, PA, 1995, pp. 287-310.
6. D.H. Hou, J. Shyue, S.S. Yang, and H.L. Fraser: in *Alloy Modeling and Design*, G.M. Stocks and P.Z.A. Turch, eds., TMS, 1994, pp. 291-8.
7. H.L. Fraser: "Research and Development of High Temperature Nb Aluminides for Component Application," Research Report, *Office of Naval Research*, Arlington, VA, 1996.
8. C.M. Austen, J.R. Dobbs, H.L. Fraser, and D. Konitzer: "Rapidly Solidified Oxidation Resistant Niobium Base Alloys," Report No. WL-TR-93-4059, Wright Laboratories, Wright-Patterson Air Force Base, Dayton, OH, 1992, p. 70.
9. B.V. Cockeram, H.J. Schmutzler, J. Shyue, K. Hoshino, S. Meng, R. Wheeler, and H.L. Fraser: *Proc. Symp. of High Temperature Ordered Intermetallic Materials—VI*, A. Horton, S. Hanada, I. Baker, R.D. Noebe, and D.S. Schwartz, eds., Materials Research Society, Pittsburgh, PA, 1994, pp. 1327-32.
10. D. Farkas: Virginia Polytechnic Institute and State University, Blacksburg, VA, unpublished research 1997.
11. J. DiPasquale, D. Gahutu, D. Konitzer, and W.O. Soboyejo: in *Fatigue and Fracture of Ordered Intermetallic Materials II*, W.O. Soboyejo, T.S. Srivatsan, and R.O. Ritchie eds., TMS, Warrendale, PA, 1996, pp. 167-178.
12. W.A. Zinnser and J.J. Lewandowski: *Metall. Mater. Trans. A*, 1998, vol. 29A, pp. 1749-57.
13. W.A. Zinnser and J.J. Lewandowski: *Scripta Mater.*, 1998, vol. 38 (12), pp. 1775-80.
14. B.P. Bewlay, J.J. Lewandowksi, and M.R. Jackson: *J. Met.*, 1997, Aug., pp. 44-67.
15. P.R. Subramanian, M.G. Mendiratta, and D.M. Dimiduk: *J. Met.*, 1996, Jan., pp. 33-38.
16. D.L. Davidson, K.S. Chan, and D.L. Anton: *Metall. Mater. Trans A*, 1996, vol. 27A, pp. 3007-18.
17. D.L. Davidson, K.S. Chan, and D.L. Anton: *Metall. Mater. Trans A*, 1997, vol. 28A, pp. 1797-1808.
18. "Standard Test Methods for Measurement of Fatigue Crack Growth Rates," ASTM E-647, ASTM, Philadelphia, PA, 1993, vol. 03.01.
19. J. Knott: *Fundamentals of Fracture Mechanics*, Butterworth, Oxford, United Kingdom, 1973.
20. G.R. Yoder, L.A. Cooley, and T.W. Crooker: *Metall. and Co. Trans. A*, 1977, vol. 8A, pp. 1737-43.
21. C. Mercer and W.O. Soboyejo: in *Superalloys 718, 625, 706 and Various Derivatives*, E.A. Loria, ed., TMS, Warrendale, PA, 1997, pp. 577-86.
22. N. Polvanich and K. Salama: *ASTM STP 962*, L. Raymond, ed., ASTM, Philadelphia, PA, 1987, pp. 417-27.
23. S. Suresh and R.O. Ritchie: in *Fatigue Crack Growth Threshold Concepts*, D.L. Davidson and S. Suresh, eds., TMS, Warrendale, PA, 1984, pp. 227-61.
24. S. Suresh: *Fatigue of Materials*, 2nd ed., Cambridge University Press, Cambridge, United Kingdom, 1998.
25. B. Rabeeh, S. Rokhlin, and W.O. Soboyejo: *Scripta Mater.*, 1996, vol. 35, pp. 1429-34.
26. P. Neumann: *Acta Metall.*, 1969, vol. 17, pp. 1219-29.
27. H.W. Liu: *Trans. Am. Soc. Mech. Eng.*, 1961, vol. 83, pp. 23-30.
28. S. Dubey, A.B.O. Soboyejo, and W.O. Soboyejo: *Acta Metall. Mater.*, 1997, vol. 45, pp. 2777-87.